Draft version July 27, 2010
Preprint typeset using LaTeX style emulateapj v. 11/10/09

arXiv:1007.4545v1 [astro-ph.SR] 26 Jul 2010

POPULATION SYNTHESIS OF COMMON ENVELOPE MERGERS: I. GIANT STARS WITH STELLAR OR SUBSTELLAR COMPANIONS

Michael Politano
Department of Physics, Marquette University, P.O. Box 1881, Milwaukee, WI 53201-1881

Marc van der Sluys[1,2]
Department of Physics, University of Alberta, 11322 - 89 Ave, Edmonton AB, T6G 2G7, Canada

and

Ronald E. Taam[3], and Bart Willems
Department of Physics and Astronomy, Northwestern University, 2131 Tech Drive, Evanston, IL 60208

Draft version July 27, 2010

ABSTRACT

Using a population synthesis technique, we have calculated detailed models of the present-day field population of objects that have resulted from the merger of a giant primary and a main-sequence or brown dwarf secondary during common-envelope evolution. We used a grid of 116 stellar and 32 low-mass/brown dwarf models, a crude model of the merger process, and followed the angular momentum evolution of the binary orbit and the primary's rotation prior to merger, as well as the merged object's rotation after the merger. We find that present-day merged objects that are observable as giant stars or core-helium burning stars in our model population constitute between 0.24% and 0.33% of the initial population of ZAMS binaries, depending upon the input parameters chosen. The median projected rotational velocity of these merged objects is $\sim 16\,\mathrm{km\,sec^{-1}}$, an order of magnitude higher than the median projected rotational velocity in a model population of normal single stars calculated using the same stellar models and initial mass function. The masses of the merged objects are typically less than $\sim 2\,M_\odot$, with a median mass of $1.28\,M_\odot$, which is slightly more than, but not significantly different from, their normal single star counterparts. The luminosities in our merged object population range from $\sim 10-100\,L_\odot$, with a strong peak in the luminosity distribution at $\sim 60\,L_\odot$, since the majority of the merged objects (57%) lie on the horizontal branch at the present epoch. The results of our population synthesis study are discussed in terms of possible observational counterparts either directly involving the high rotational velocity of the merger product or indirectly, via the effect of rotation on envelope abundances and on the amount and distribution of circumstellar matter.

Subject headings: binaries: close — circumstellar material — stars: horizontal branch — stars: rotation

1. INTRODUCTION

There is a general consensus that the common-envelope (CE) phase plays an essential role in the evolution of many close binary stars. During CE evolution, one star becomes engulfed in the envelope of its companion. The orbit of the binary decays due to the action of gravitational torques (*e.g.*, Ricker & Taam 2008) between it and the non-co-rotating envelope. CE evolution involving stars in various evolutionary states can occur, but the ultimate fate of such evolution, regardless of the states of the component stars, is either a merger or a stable binary system (see Iben & Livio 1993; Taam & Sandquist 2000, for reviews).

There has been a renewed interest in CE mergers, specifically in massive binaries where merger of the cores or of a core and in-spiraling compact object has been suggested as a mechanism for producing hypernovae and gamma-ray bursts (*e.g.*, Fryer & Woosley 1998; Middleditch 2004; Fryer & Heger 2005). In this paper, we investigate the evolutionary consequences of CE mergers involving lower-mass binaries consisting of a low- to intermediate-mass giant star and a stellar or substellar companion. Research on CE evolution involving low-mass binaries has focused almost exclusively on systems that survive CE evolution. In part, this is due to the identification of observational counterparts to such surviving systems (*e.g.*, cataclysmic variables, double degenerate white dwarfs) and the lack of such obvious counterparts to mergers. However, detailed hydrodynamical calculations of CE evolution, incomplete as they are, indicate that mergers should occur in such systems (*e.g.*, Sandquist et al. 1998; Sandquist, Taam, & Burkert 2000). Furthermore, population synthesis of close binary stars that involve a single phase of CE evolution between a low- to intermediate-mass giant star and a stellar or substellar companion predict that mergers should be as frequent as post-CE binaries in the disk of our Galaxy (Politano & Weiler 2007). Such studies suggest that there may exist a significant number of merged objects in our Galaxy that have yet to be recognized as such observationally.

Only a handful of studies of the consequences of CE mergers in low-mass binaries exist in the literature. Podsiadlowski (2001) provides an overview of some of the

---

[1] CITA National Fellow
[2] Department of Physics and Astronomy, Northwestern University, 2131 Tech Drive, Evanston, IL 60208
[3] Academia Sinica Institute of Astronomy & Astrophysics/TIARA, Taipei, Taiwan

physical considerations involved in modeling CE mergers in general. Siess & Livio (1999a,b), Soker & Harpaz (2000, 2007), and Carlberg, Majewski, & Arras (2009) investigated the spiral-in and evaporation of planets or brown dwarfs (BDs) inside the envelope of a giant star. These authors found that the result of such a merger is a rapidly rotating single star, and they suggest that such mergers could explain certain abundance anomalies, such as enhanced Li, observed in the envelopes of a small fraction of giant stars, as well as the heterogeneity found among horizontal branch (HB) stars. Blue stragglers, single subdwarf B (sdB) or subdwarf O (sdO) stars, and R Coronae Borealis stars, to name a few, have been suggested as possible observational counterparts to low-mass CE mergers (*e.g.*, Tutukov & Yungleson 2005; Soker & Harpaz 2007; Politano et al. 2008). However, there have been only two population synthesis studies that explored the consequences of low-mass CE mergers: Izzard, Jeffery, & Lattanzio (2007), who modeled the population of early-type R stars, and Politano et al. (2008), who modeled the population of single sdB stars.

In this paper, we extend our previous work (Politano et al. 2008) and present population synthesis calculations of the present-day population of objects in the disk of our Galaxy that have resulted from mergers during a single phase of CE evolution involving a giant primary and a stellar or substellar secondary. To the best of our knowledge, these are the first population synthesis calculations that comprehensively explore the consequences of mergers that occur during CE evolution involving low-mass binaries. In § 2, we describe the method used to model this population and discuss the assumptions underlying our study. In § 3, the results of our calculations are presented and compared to a corresponding present-day population of normal single stars calculated using the same grid of stellar-evolution models. In § 4, we discuss the observational signatures of CE mergers and speculate about potential observational counterparts to CE mergers. Finally, we summarize and conclude in the last section (§ 5).

2. METHOD

2.1. *Population synthesis code*

We use the Monte-Carlo population synthesis code developed by Politano (Politano 1996; Politano & Weiler 2007) with two major modifications: (1) the analytic fits that had been used previously (see Politano 1996) have been replaced by numerical tables of 116 up-to-date stellar models ranging in mass from 0.5 to 10.0 $M_\odot$ in increments of 0.1 $M_\odot$ and from 10.5 to 20 $M_\odot$ in increments of 0.5 $M_\odot$ and (2) tidal effects which act to synchronize the rotation of the primary with the orbital motion of the system have been included.

The updated stellar models were calculated using a version of the binary stellar evolution code `ev`[4] developed by Eggleton (Eggleton 1971, 1972; Yakut & Eggleton 2005, and references therein) and updated as described in Pols et al. (1995). Convective mixing is modelled by a diffusion equation, using a mixing-length to pressure scale-height ratio $l/H_\mathrm{p} = 2.0$. Convective overshooting in the core is taken into account on the main sequence for stars with $M \gtrsim 1.2\,M_\odot$ and on the horizontal branch for stars of all masses. We use an overshooting parameter $\delta_\mathrm{ov} = 0.12$, which corresponds to an overshooting length of about $0.3\,H_\mathrm{p}$. The code cannot evolve a model through the helium flash, but this is resolved by automatically replacing the model at the moment of degenerate helium ignition by a tailored model with the same total mass and core mass in which helium was just ignited non-degenerately. For stars with $M \gtrsim 2.1\,M_\odot$, helium ignites non-degenerately and this intervention is not needed. The helium-core mass M_c is defined as the mass coordinate at which the hydrogen abundance drops below 10%. We compute the binding energy of the hydrogen-rich envelope, E_bind, by integrating the gravitational and internal energies over the mass coordinate of the model, from the core-envelope boundary to the surface of the star. In the internal energy we include the thermal energy, but not the recombination energy. More details regarding these assumptions are provided in van der Sluys et al. (2006). The initial composition of our model stars is $X = 0.70$, $Y = 0.28$ and $Z = 0.02$. Mass loss via stellar winds is incorporated in the models using a prescription that was originally inspired by Reimers (1975):

$$\dot{M} = -\eta \times \min \begin{cases} 3.16\times10^{-14} M_\odot\,\mathrm{yr}^{-1} \left(\frac{M}{M_\odot}\right)\left(\frac{L}{L_\odot}\right)\left(\frac{E_\mathrm{bind}}{10^{50}\mathrm{erg}}\right)^{-1} \\ 9.61\times10^{-10} M_\odot\,\mathrm{yr}^{-1} \left(\frac{L}{L_\odot}\right) \end{cases}, \tag{1}$$

where we use $\eta = 0.2$ in this study, and the prescription by de Jager et al. (1988), which is negligible except for the most massive stars in our grid. The upper prescription in Eq. 1 is used in the majority of our models, except where the envelope binding energy is small (in absolute value), *e.g.*, for stars near the tip of the asymptotic giant branch (AGB).

As a second modification, we now assume synchronism of the primary's rotation with the orbital motion whenever the primary is on either giant branch. In these cases, after each time step, the new total angular momentum of the system is calculated, accounting for losses due to stellar winds. Synchronism is then enforced by redistributing this total angular momentum, J_tot, such that the rotational angular velocity of the primary is equal to the orbital angular velocity of the binary. The new orbital separation is calculated as the root of the following equation:

$$z^4 - bz^3 + c = 0. \tag{2}$$

In this equation, $z = (a/R)^{1/2}$, where a is the orbital separation and R is the primary's radius, and b and c are dimensionless constants given by $b = J_\mathrm{tot}/[G\mu^2(M_\mathrm{p}+M_\mathrm{s})R]^{1/2}$ and $c = k^2(1+M_\mathrm{p}/M_\mathrm{s})$, where G is the universal gravitation constant, M_p and M_s are the primary and secondary masses, respectively, μ is the reduced mass of the binary, and k is the radius of gyration of the primary. In all cases, the rotational angular momentum of the secondary is neglected and a circular orbit and rigid-body rotation for the primary are assumed.

In our population synthesis calculations, we begin with 10^7 zero-age main sequence (ZAMS) binaries. We assume that these binaries are distributed over primary mass

---

[4] The current version of `ev` is obtainable on request from `eggleton1@llnl.gov`, along with data files and a user manual.

($M_{\rm p}$) according to a Miller & Scalo (1979) initial-mass function (IMF), over orbital period uniformly in $\log P$ (Abt 1983) and over mass ratios uniformly in q (*i.e.*, $g(q)\,dq = 1\,dq$, Duquennoy & Mayor 1991; Mazeh et al. 1992; Goldberg et al. 2003), where $q = M_{\rm s}/M_{\rm p}$. Given the large observational uncertainties in the distribution of mass ratios in ZAMS binaries, we also investigate the dependence of our results on the assumed choice for $g(q)$ (see § 2.4). We adopt a minimum primary mass of $0.95\,M_\odot$, a maximum primary mass of $10\,M_\odot$ and a minimum secondary mass of $0.013\,M_\odot$ in our calculations. For secondaries with masses less than $0.5\,M_\odot$, including substellar secondaries, we use detailed stellar models from the Lyon group (Chabrier & Baraffe 1997; Baraffe et al. 1998, 2003; Chabrier et al. 2000). For secondaries with masses greater than or equal to $0.5\,M_\odot$, we use the same stellar models as for the primary. We assume that the CE phase is so rapid that its duration is negligible compared to the other time scales (*e.g.*, Iben & Livio 1993; Taam & Sandquist 2000), the age of the Galaxy is 10^{10} yrs (representative of the thin-disk population), and the star formation rate throughout the Galaxy's history has remained constant. Lastly, we do not take into account angular momentum loss due to magnetic braking.

2.2. *Merger scenario*

To model the population of mergers between giant primaries and less massive companions, we adopt the following scenario. A given ZAMS binary is evolved until the primary reaches the base of the red-giant branch (RGB), at which point synchronism between the primary's rotation and the orbit is assumed. As the primary ascends the RGB, two conditions are checked at the end of each time step: (1) has the primary filled its Roche lobe or (2) has a tidal instability developed (see below). If the Roche lobe has been filled, we check to see if the mass transfer will be unstable by using the criterion given in Hurley et al. (2002) (their Eq. 57):

$$q_{\rm crit} = \frac{2.13}{1.67 - x + 2(M_{\rm c}/M_{\rm p})^5}, \qquad (3)$$

where $M_{\rm p}$ and $M_{\rm c}$ are the total mass and core mass of the primary when it fills its Roche lobe and $x = 0.30$ if $M_{\rm c} \leq 0.50\,M_\odot$ or $x = 0.33$ if $M_{\rm c} > 0.50\,M_\odot$. If $q < q_{\rm crit}$, the mass transfer will be unstable and a CE phase will ensue. If $q > q_{\rm crit}$, the mass transfer will be stable and the system will avoid a CE phase. The evolution of such systems is no longer followed and these systems are removed from the population[5]. If a tidal instability has developed, we assume a CE phase will inevitably ensue.

If the primary does not fill its Roche lobe or if a tidal instability does not develop on the RGB, the primary is evolved through the core He-burning phase and then resynchronized at the base of the AGB. As the primary ascends the AGB, the same two conditions as before are checked at the end of each time step and the same procedure is followed. If neither condition is satisfied when the primary reaches the tip of the AGB, the system is removed from the population.

To determine if merger occurs within the CE, simple energy considerations are used to relate the pre- and post-CE orbital separations (Tutukov & Yungleson 1979). Although the exact prescription varies somewhat depending upon the author, a typical expression used in population synthesis calculations is given below (*e.g.*, Iben & Tutukov 1985; Politano 1996; Willems et al. 2005)

$$-\,\alpha_{\rm CE}\left(\frac{GM_{\rm c}M_{\rm s}}{2a_{\rm f}} - \frac{GM_{\rm p}M_{\rm s}}{2a_{\rm i}}\right) = E_{\rm bind,i}, \qquad (4)$$

where $a_{\rm i}$ and $a_{\rm f}$ are the pre- and post-CE orbital separations, respectively, $E_{\rm bind,i}$ is the binding energy of the primary's envelope at the onset of the CE phase, and $\alpha_{\rm CE}$ is a parameter that measures the efficiency with which orbital energy is transferred to the CE. The parameter $\alpha_{\rm CE}$ embodies a major uncertainty in this simplified prescription. We have chosen $\alpha_{\rm CE} = 1$ as our standard model and we investigate the dependence of our results on $\alpha_{\rm CE}$ (see § 2.4). The term $E_{\rm bind,i}$ includes both the gravitational binding energy and thermal internal energy of primary's envelope, and is computed directly from the detailed stellar-structure models. We note that this eliminates the need to parametrize the envelope's binding energy using a dimensionless constant, λ (*i.e.*, $E_{\rm bind,i} = GM_{\rm e}[M_{\rm e} + M_{\rm c}]/\lambda R_{\rm i}$, where $M_{\rm e}$ and $R_{\rm i}$ are the envelope mass and radius of the primary at the onset of the CE phase). Merger is assumed to have occurred if the radius of the secondary is larger than its Roche-lobe radius at the end of the CE phase.

We also consider mergers that result from a tidal instability. If the moment of inertia of the primary exceeds one-third of the moment of inertia of the binary orbit before the primary fills its Roche lobe on the RGB or AGB, Eq. 2 has no real roots. Physically, this implies that there will no longer be sufficient angular momentum within the orbit to keep the envelope rotating synchronously (Darwin 1879) and the orbit will continue to shrink until mass transfer starts, after which either the envelope is ejected or a merger occurs.

2.2.1. *Treatment of the merger process*

Available detailed hydrodynamical models of stellar mergers have focused on collisions between stars and are more appropriate for mergers that occur as a result of stellar interactions within dense stellar environments, such as at the centers of globular clusters (*e.g.*, Sills et al. 1997, 2001; Lombardi et al. 2002). In the absence of detailed models that are applicable to stellar mergers during CE evolution, a very simplified model for the merger process is adopted. The key assumptions underlying our treatment are listed below.

1. In most cases, the merger of part or all of the secondary with the primary leads to an object spinning at several times its break-up rotational velocity, given by $v_{\rm br} = (GM/R)^{1/2}$, where M and R are the object's mass and radius, respectively. Consequently, we assume that a rapid mass-loss phase occurs when the rotational velocity of the object exceeds some critical rotational velocity,

---

[5] We recognize that such systems may potentially undergo a CE phase later in their evolution (*e.g.*, if unstable mass transfer is initiated when the secondary fills its Roche lobe). However, our code does not treat phases of stable mass transfer.

$v_{\rm crit} = \beta\, v_{\rm br}$. For our standard model, we assume $\beta = 1/3$, which corresponds to centrifugal forces contributing about 10% of the force against gravity. Our choice is motivated by the fact that we have adopted mass loss rates for single stars, including giant stars, that are slowly rotating. At higher rotational velocities, it is likely that strong magnetic activity would be present, significantly enhancing the mass loss rates. The rate of mass loss via such a process is not well understood, and we have adopted standard rates to avoid introducing an additional parameter in this preliminary study. To explore the qualitative effect of the choice of β on our results, we calculated model populations for other values of β (see § 2.4).

2. The merged object is assumed to assimilate only as much mass from the binary as is required such that it rotates at the critical velocity specified under 1, and we assume that the remaining mass is expelled from the system. We note that the latter is a simplifying assumption. In reality, it may be that only a portion of this remaining mass actually has enough energy to escape from the system, with the rest eventually accreted by the merged object (likely through an accretion disk).

3. The material in the merged object is assumed to be grossly distributed according to its specific entropy, with lower-entropy material residing in the core and higher-entropy material residing in the envelope. Consequently, we assume that the merged object has a core mass that is equal to that of the original primary, but an envelope mass that is potentially larger than that of the primary.

4. Although the merged object is unlikely to be in a state of thermal equilibrium initially, we assume for definiteness that the radius of the merged object corresponds to that of a star in the model grid for the same core mass and total mass after it achieves thermal equilibrium. Such an approximation may underestimate the amount of angular momentum that the remnant may acquire immediately after the merger process, which could lead to an increased level of magnetic activity due to dynamo action and an elevated level of mass and angular momentum loss (see item 1 above).

5. In some cases, the merger results in an object with a total mass/core mass combination for which no corresponding giant-branch model exists in our stellar grid. In the majority of these cases, the core mass of the merged object is less than the core mass at the base of the corresponding giant branch for a stellar model with the same total mass. Rather than permit an unphysical evolutionary regression, such as an AGB primary reverting to a core He-burning star as a result of the merger, we choose the stellar model in our grid at the base of the corresponding giant branch with the same total mass as the merged object. Clearly this is not optimal, but the difference in core mass is generally small and, at present, we can do no better.

6. If the CE takes place when the primary is on the RGB, the merger may result in a total-mass/core-mass combination that corresponds to a core-He burning star in our model grid (i.e., since the critical core mass for degenerate He ignition decreases with increasing total mass, the additional envelope material acquired during merger may reduce the critical core mass needed for He ignition). Since it is physically reasonable for an RGB star to ignite helium in the core, even if induced by a merger event, we adopt a core He-burning model for the merged object.

2.3. *Evolution of the merged object to the present epoch*

The subsequent evolution of the merged object, including its rotational velocity, $v_{\rm rot}$, is followed until the present epoch using the same grid of stellar evolution models that we used for the primary prior to merger. In addition to angular momentum loss due to stellar winds, we assume that angular momentum is removed from the merged object's envelope via rotationally enhanced mass loss whenever $v_{\rm rot}$ exceeds $v_{\rm crit}$. Typically, this occurs when there is a significant decrease in the merged object's radius, such as during contraction to the HB following He ignition. If $v_{\rm rot} > v_{\rm crit}$ during a given time step, we calculate the amount of angular momentum that needs to be lost so that the merged object will rotate exactly at $v_{\rm crit}$ and we artificially remove the corresponding amount of mass from the envelope. Once $0.1\,M_\odot$ of material is lost, it becomes necessary to shift to the next lowest-mass model in our grid with the same core mass in order to continue to follow the object's evolution. If there is no corresponding lower-mass model with the same core mass, we follow the procedure described in assumption 5 in the previous section. However, in some cases this procedure proved unsatisfactory and led to unphysical behavior. For example, some objects would continue to lose mass, moving along the base of the HB until the object moved off the grid. To address this, we softened our condition for shifting to the next lowest-mass model by letting the object evolve for five additional time steps before shifting. We found that if the object's rotational velocity dropped below critical during these five time steps, its rotational velocity stabilized and the evolution could generally be followed for the remainder of its evolution without problem. If the merged object completes its evolution as an AGB star before the present epoch is reached, we assume it will be a white dwarf at the present epoch, and we remove the object from the population.

2.4. *Input parameters*

For our standard model, we have assumed values for the CE efficiency parameter and ZAMS mass ratio distribution that are common in the literature, namely, $\alpha_{\rm CE} = 1$ and $g(q)\,dq = 1\,dq$. In addition, we have chosen a value of $\beta = 1/3$ in our standard model, where the parameter β represents the fraction of the break-up velocity for which we assume rotationally-induce mass transfer begins (see item 1 of § 2.2.1). Given the large uncertainties in these parameters, we have calculated model populations for other choices of these parameters. We list the parameter choices made for each model in Table 1.

Table 1
Input parameter choices for the models in this study

Model	$\alpha_{\rm CE}$	$g(q)$	β
standard	1.0	1	$\frac{1}{3}$
$\alpha_{\rm CE} = 0.5$	0.5	1	$\frac{1}{3}$
$\alpha_{\rm CE} = 0.1$	0.1	1	$\frac{1}{3}$
$g(q) = q$	1.0	q	$\frac{1}{3}$
$g(q) = q^{-0.9}$	1.0	$q^{-0.9}$	$\frac{1}{3}$
$v_{\rm crit} = v_{\rm br}$	1.0	1	1.0
$v_{\rm crit} = 0.1\,v_{\rm br}$	1.0	1	0.1

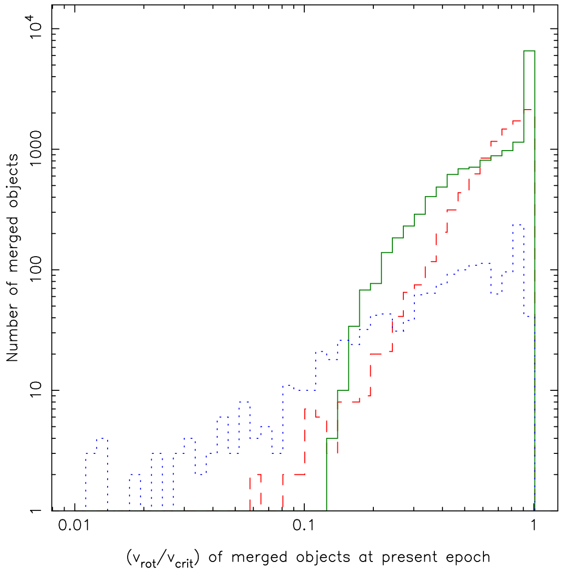

Figure 1. Distribution of the rotational velocities in our standard model population of present-day merged objects for three subpopulations: RGB stars (dashed curve), HB stars (solid curve) and AGB stars (dotted curve). The horizontal axis shows the rotational velocity as a fraction of the critical rotational velocity, $v_{\rm crit}$, which is assumed to be $\frac{1}{3}$ of the break-up velocity (see text).

3. RESULTS

In this section, we present the results of our population synthesis calculations. In § 3.1, we discuss the general characteristics of the present-day population of merged objects, with an emphasis on observable quantities such as rotational velocity, luminosity, effective temperature, etc. All results in § 3.1 are for our standard model (see Table 1). In § 3.2, we discuss the dependence of our results on other choices for these three parameters, as listed in Table 1. Finally, in § 3.3, we compare our model population of merged objects with a standard single-star population calculated from the same set of stellar evolutionary models.

3.1. *Properties of present-day population of merged objects*

3.1.1. *Relative numbers and sub-populations*

In our population synthesis calculations, we consider a population of 10^7 primordial binaries with initial properties as described in § 2.1. In our standard model, $\sim 71\%$ of these binaries never initiate mass transfer, 13% undergo stable mass transfer and 16% undergo unstable mass transfer, which leads to a CE phase. Of those binaries undergoing CE evolution, 48% survive the CE phase, while 52% merge (8.5% of the original population). 82% of the CEs are formed when the primary fills its Roche lobe, whereas 18% undergo a Darwin instability. Furthermore, 87% of the mergers occur when the primary is on the RGB, while 13% occur when the primary is on the AGB.

In the evolution following merger, the vast majority (97%) of the merged objects will have evolved beyond the AGB by the present epoch. These merger remnants would be observed as white dwarfs today and are not included in our present-day population of merged objects. Only 3% of the merged objects ($\sim 25,000$ stars or 0.25% of our original population) would be observed as non-degenerate stars today. The properties of these 25,000 merged objects are listed in Table 2.

We have divided the total population of 25,000 present-day merged objects into three sub-populations: RGB stars, HB stars and AGB stars. The properties of each of these sub-populations are also listed in Table 2. We find that HB stars are the most numerous in our present-day population (57%), followed by RGB stars (37%) and then AGB stars (6%). This can be understood intuitively from the fact that of the merger remnants observed today, 99.9% were formed in a merger on the RGB, compared to 0.1% for which the merger took place on the AGB. In particular, we find that mergers during CE evolution typically occur in binaries with primary masses of $\sim 1 - 2\,M_\odot$ that fill their Roche lobes on the lower half of the RGB at orbital periods between roughly 1 and 30 days. The distribution of mass ratios at the onset of the CE phase is almost uniform between 0 and 1. While RGB mergers produce remnants that must evolve through the rest of the RGB phase, the relatively long-lasting HB phase and the AGB phase, AGB mergers produce remnants that evolve off the AGB quickly and disappear from our present-day population. Of all the RGB mergers, only 2.4% of the remnants ignite helium in the core and become HB stars as an immediate consequence of the merger. Most of the remaining RGB mergers will have evolved off the RGB by the time of the present epoch, and the distribution of stars over the three branches is to a large extent determined by the relative lifetimes of the stars in each phase.

3.1.2. *Rotational velocity*

In Fig. 1, we show the predicted distribution of present-day rotational velocities in our model population of merged objects for the three sub-populations: RGB stars (red/dashed), HB stars (green/solid) and AGB stars (blue/dotted). The rotational velocity is given as a fraction of an assumed critical velocity for rotational mass loss, $v_{\rm crit}$ (see § 2.2.1). For our standard model, $v_{\rm crit} = 14.6\,{\rm km\,s^{-1}}(M/M_\odot)^{1/2}(R/100\,R_\odot)^{-1/2}$.

We find that the distributions for the AGB, RGB and HB, respectively, are increasingly peaked towards high $v_{\rm rot}$. This occurs because most of the stars are on the RGB directly after merger and are rotating rapidly. During the evolution on the remainder of the RGB, the rotation of the stars will slow down due to their nuclear evolutionary expansion. When helium ignites in the core, the merged objects evolve to the HB, which causes them

Table 2
Dependence of selected model results upon input parameters

Model	N[a]	$\frac{N}{N_{\rm tot}}$[b]	M[c] ($M_\odot$)	$v \sin i$[d] (km/s)	Fraction with[e] $v_{\rm rot} \leq 0.1\, v_{\rm crit}$	$v_{\rm rot} = v_{\rm crit}$	$M_{\rm rej}$[f] ($M_\odot$)	$\frac{M_{\rm rej}}{M_{\rm bin}}$[g]	$\frac{\Delta M_{\rm mrg}}{M_{\rm mrg,i}}$[h]
RGB stars									
standard	9301	0.37	1.20	18.4	(0.001)	0.0319	0.63	0.34	0.00
$\alpha_{\rm CE} = 0.5$	9534	0.34	1.20	17.7	(0.0009)	0.0343	0.64	0.34	0.00
$\alpha_{\rm CE} = 0.1$	9634	0.29	1.20	17.4	(0.0009)	0.0363	0.64	0.34	0.00
$g(q) = q$	9044	0.36	1.20	18.2	(0.0009)	0.0368	0.89	0.42	0.00
$g(q) = q^{-0.9}$	8819	0.35	1.20	18.4	(0.0007)	0.0251	0.16	0.11	0.00
$v_{\rm crit} = v_{\rm br}$	8025	0.33	1.30	48.7	(0.0006)	0.0179	0.45	0.25	0.00
$v_{\rm crit} = 0.1\, v_{\rm br}$	9783	0.38	1.19	5.4	(0.001)	0.0250	0.71	0.37	0.00
single stars	178651	0.61	1.20	1.9	0.9627	0.000	...	...	...
HB stars									
standard	14305	0.57	1.35	16.1	(0.0000)	0.3149	0.93	0.40	0.12
$\alpha_{\rm CE} = 0.5$	16987	0.60	1.34	16.7	(0.0000)	0.3469	0.91	0.41	0.12
$\alpha_{\rm CE} = 0.1$	21043	0.64	1.23	17.3	(0.0000)	0.4091	0.91	0.42	0.13
$g(q) = q$	14267	0.57	1.35	16.1	(0.0000)	0.3275	1.25	0.49	0.12
$g(q) = q^{-0.9}$	14929	0.59	1.35	16.5	(0.0000)	0.3264	0.32	0.20	0.11
$v_{\rm crit} = v_{\rm br}$	14943	0.61	1.58	50.5	(0.0004)	0.2098	0.74	0.32	0.08
$v_{\rm crit} = 0.1\, v_{\rm br}$	14217	0.56	1.24	4.5	(0.0008)	0.3366	1.03	0.44	0.12
single stars	104979	0.36	1.58	3.2	0.0886	0.0021	...	...	...
AGB stars									
standard	1435	0.06	1.34	6.0	0.0683	(0.0007)	0.94	0.42	0.13
$\alpha_{\rm CE} = 0.5$	1748	0.06	1.31	6.3	0.0732	(0.0011)	0.94	0.42	0.13
$\alpha_{\rm CE} = 0.1$	2205	0.07	1.23	6.4	0.0757	(0.0018)	0.92	0.43	0.14
$g(q) = q$	1542	0.06	1.34	6.4	0.0746	(0.0013)	1.27	0.49	0.13
$g(q) = q^{-0.9}$	1595	0.06	1.34	6.0	0.0678	(0.0031)	0.36	0.23	0.12
$v_{\rm crit} = v_{\rm br}$	1446	0.06	1.56	18.7	0.0788	(0.0007)	0.74	0.33	0.09
$v_{\rm crit} = 0.1\, v_{\rm br}$	1490	0.06	1.23	1.8	0.0859	(0.0007)	1.09	0.46	0.14
single stars	10487	0.04	1.45	1.3	0.5657	(0.0000)	...	...	...
Total population									
standard	25041	1.00	1.28	16.2	0.0043	0.1918	0.81	0.38	0.07
$\alpha_{\rm CE} = 0.5$	28269	1.00	1.23	16.2	0.0048	0.2201	0.81	0.38	0.08
$\alpha_{\rm CE} = 0.1$	32882	1.00	1.23	16.5	0.0054	0.2726	0.83	0.40	0.10
$g(q) = q$	24853	1.00	1.29	16.0	0.0049	0.2015	1.10	0.46	0.07
$g(q) = q^{-0.9}$	25343	1.00	1.29	16.3	0.0045	0.2012	0.28	0.18	0.07
$v_{\rm crit} = v_{\rm br}$	24414	1.00	1.46	47.7	0.0051	0.1343	0.63	0.30	0.02
$v_{\rm crit} = 0.1\, v_{\rm br}$	25490	1.00	1.20	4.6	0.0058	0.1974	0.90	0.41	0.08
single stars	294117	1.00	1.23	2.3	0.6366	0.0008	...	...	...

Note. — Entries enclosed by parentheses indicate the number of objects is so small as to not be statistically significant.

[a] total number of merged objects in present-day population

[b] fraction of present-day population in this evolutionary state

[c] median mass of merged objects in present-day population

[d] median projected rotational velocity of merged objects in present-day population

[e] fraction of merged objects in present-day population rotating at one-tenth of the critical velocity or less and at the critical velocity (defined in § 2.2.1)

[f] median amount of mass that is not accreted by the remnant during merger

[g] same as f, except given as a fraction of the total mass of the binary at the onset of the CE phase

[h] median of the relative difference between the mass immediately after the merger event, $M_{\rm mrg,i}$, and the mass at the present epoch, $M_{\rm mrg,PE}$: $\frac{M_{\rm mrg,i} - M_{\rm mrg,PE}}{M_{\rm mrg,i}}$

to shrink and increase their rotational velocities. Many of these stars will reach critical rotation while shrinking, thus forcing them to lose mass and angular momentum as described in § 2.3. These stars will arrive on the HB spinning critically, causing the peak at $\log(v_{\rm rot}/v_{\rm crit}) \approx 0$. Since HB stars do not expand dramatically during the core helium burning phase, many will be found at or close to this peak. When these stars continue their evolution on the AGB, they will be spinning less rapidly than they were on the RGB at a similar radius, because of angular momentum loss during the intervening evolution. In fact, of the three sub-populations, there exists a relatively sharp lower cutoff in rotational velocities at $0.1\, v_{\rm crit}$ for both the HB and RGB stars, whereas the AGB stars show a smooth decline. For merged objects that are AGB stars at the present epoch, we find that 98% were formed through a merger on the RGB, while only 2% actually merged on the AGB.

To facilitate comparison with observations, Figure 2a shows the same distributions as Fig. 1, but with the velocity converted to a physical equatorial velocity in $\mathrm{km\,s^{-1}}$. In addition, in Fig. 2b we have computed the projected rotational velocity, $v\sin i$, as could be inferred from spectroscopic observations. We used a uniform distribution in $\sin i$ to generate a random inclination for each of our merger remnants. Whereas most late-type giant stars are observed to rotate with projected velocities of a few $\mathrm{km\,s^{-1}}$ (*e.g.*, Carlberg, Majewski, & Arras 2009) — indeed our comparison model of a single-star population (see § 3.3) has a median $v\sin i$ of $2.3\,\mathrm{km\,s^{-1}}$ — we find that the median value for $v\sin i$ of the total merged population in Fig. 2b is $16.2\,\mathrm{km\,s^{-1}}$.

In Figure 3, we show an HR diagram with the distribution of the medians of the projected rotational velocities in each bin. The highest velocity stars are found at the bottom of the RGB, with physical and projected velocities in excess of $100\,\mathrm{km\,s^{-1}}$ and $80\,\mathrm{km\,s^{-1}}$, respectively. Stars on the RGB around 5000 K and on the HB still have projected velocities between 10 and $60\,\mathrm{km\,s^{-1}}$, whereas the merger products in the upper regions of the HR diagram have rotational velocities that are more common for giants (a few $\mathrm{km\,s^{-1}}$), although still faster than for single stars in that region of the HR diagram.

3.1.3. *Total mass*

In Figure 4, we show the predicted distribution of present-day total masses in our model population of merged objects for the three sub-populations: RGB stars (red/dashed), HB stars (green/solid) and AGB stars (blue/dotted). All three distributions peak at low masses and monotonically decrease towards higher mass, as may be expected. However, while the AGB distribution looks much like a scaled-down version of the HB distribution, the distribution for merged objects presently on the RGB is much narrower, with a higher low-mass cut-off and a steeper drop-off towards higher masses. This steep drop-off occurs because a low-mass star ($M \lesssim 2.1\,M_\odot$) with a degenerate helium core spends more time on the RGB than a higher-mass star ($M \gtrsim 2.1\,M_\odot$) with a non-degenerate helium core. As a consequence, of all mergers that occurred while the primary was on the RGB, 42% of them remain on the RGB at the present epoch if $M \lesssim 2.1\,M_\odot$, whereas only 1.2% of them are presently RGB stars if $M \gtrsim 2.1\,M_\odot$. As a result of this, mergers in the latter category end up as rapidly rotating HB stars about 2.5 times more frequently and have an 80% higher chance to be observed as AGB stars today than mergers in the former group. Table 2 shows that, for our standard model, the median mass of the total population is $1.28\,M_\odot$, with a clearly lower number for the RGB sub-population due to this steep drop-off.

Figure 5 displays a two-dimensional histogram of the M_{tot}–v_{rot} plane, for the total present-day population of merged objects (RGB, HB and AGB). This figure indicates that most of the merger remnants are low-mass ($\lesssim 2\,M_\odot$), rapidly rotating stars, with a peak in the distribution corresponding to a mass and velocity range of $M \approx 1.0-1.3\,M_\odot$ and $v_{\mathrm{rot}}/v_{\mathrm{crit}} \approx 0.75-1$, respectively.

3.1.4. *Luminosity*

In Fig. 6, the predicted distribution of the present-day luminosities in our model population of merged objects is illustrated. As in the previous figures, the distribution is divided into 3 sub-populations: RGB stars (red/dashed), HB stars (green/solid) and AGB stars (blue/dotted). The HB star distribution ranges in $\log L/L_\odot$ from 1.6 to $\sim$ 3 and is sharply peaked near $\log L/L_\odot = 1.8$. The RGB distribution is broader and flatter, ranging in $\log L/L_\odot$ from $\sim$ 0.4 to 3.3 and having a broad maximum near $\log L/L_\odot = 1.4$. The AGB distribution ranges in $\log L/L_\odot$ from $\sim$ 1.9 to 4.1 and has multiple maxima, with a strong peak at $\log L/L_\odot \sim 2.0$ and a weaker one near $\log L/L_\odot \sim 2.4$. We note that the strong peak in the AGB distribution lies near that of the HB distribution, thus contributing to the peak in the overall luminosity distribution.

3.1.5. *HR diagram*

In Figure 7, we show binned HR diagrams (HRDs) for the total model population of merged objects. Fig. 7a is a two-dimensional histogram, in which the grey scale indicates the number of merged objects per two-dimensional bin (pixel). If we draw an imaginary line from the upper-left to the lower-right corners of the diagram, this line intersects the distribution on the giant branches almost perpendicularly. When we start in the upper-left corner and follow this line through the distribution, we find that there is a gradient in the number density of merged objects, and that this density increases as we continue to follow the line towards the lower-right corner. This gradient is the result of the IMF; there are more lower-mass than higher-mass stars, and the evolutionary tracks of lower-mass stars on the giant branches lie to the lower right of those of higher-mass stars. In addition, we find that the majority of our merged objects sit in a dense clump at the HB (see § 3.1.2), with $T_{\mathrm{eff}} \approx 4500-5000\,\mathrm{K}$ and $L \approx 60\,L_\odot$.

Figure 7b displays the medians of the velocity distributions of merged objects in each bin of the HRD. Since the standard deviations of these distributions are almost always significantly smaller than the medians, this is a relevant estimate of the rotational velocity. Whereas the number of stars in each bin is a function of mass, the velocity is clearly dependent on evolutionary phase. Especially for the RGB, it is clear that the rotational velocity diminishes towards the tip of the giant branch. The HB contains fast rotators, as we saw earlier, and even the AGB shows a few pixels with a high rotational velocity, although Fig. 7a indicates that these pixels each contain about one star.

3.1.6. *Oblateness*

The high rotational velocities of the present-day merged objects (see § 3.1.2) may well give rise to deformation of the stars. In order to quantify the oblateness of the stars, we assumed they can be treated as MacLaurin spheroids, for which the relation between angular frequency ω, density ρ and oblateness e is given by

$$\frac{\omega}{\sqrt{2\pi G\rho}} = \left[\frac{\left(1-e^2\right)^{1/2}}{e^3}\left(3-2e^2\right)\sin^{-1}(e) - \frac{3}{e^2}\left(1-e^2\right)\right]^{1/2}, \quad (5)$$

(MacLaurin 1742), where we use $\rho = \bar{\rho}_*$, the mean density of the star, and the eccentricity or oblateness is defined in terms of the polar and equatorial radius (r_{p} and

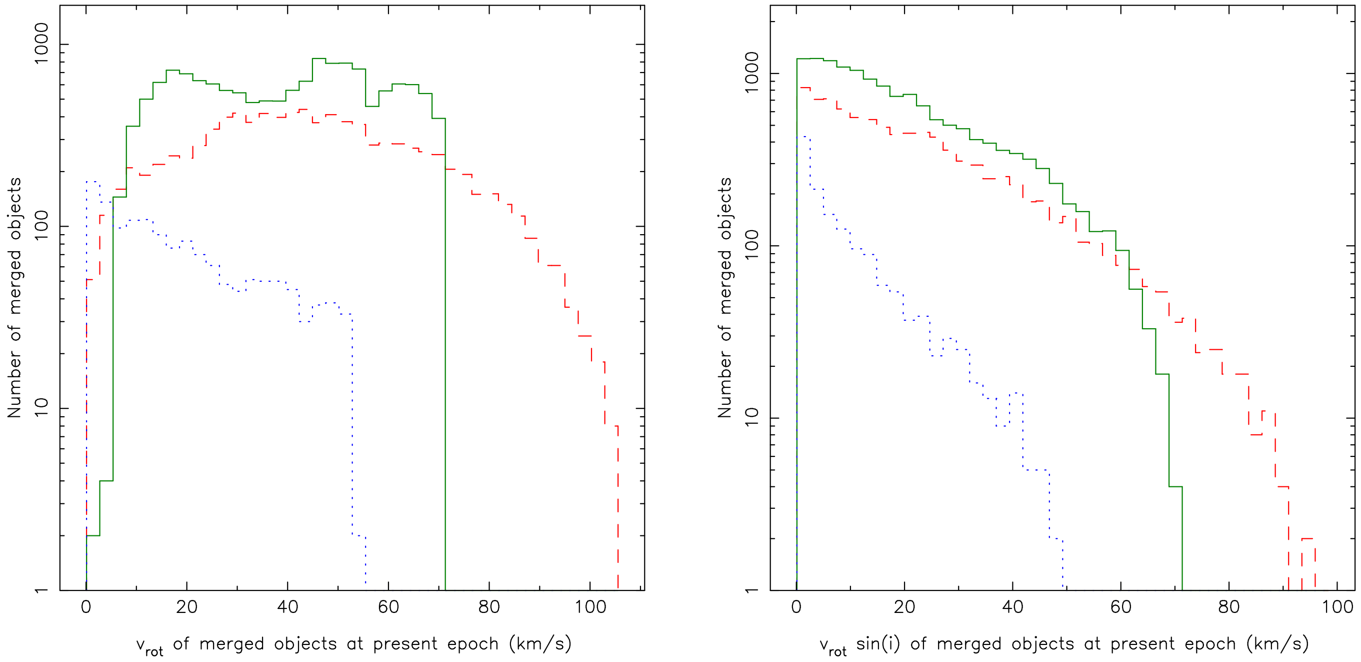

Figure 2. Histograms of the equatorial rotational velocities of the sub-populations of merged objects on the RGB (dashed curve), HB (solid curve) and AGB (dotted curve) in our standard model. The left-hand panel **(a)** shows the distributions of *physical* velocities in km/s, the right-hand panel **(b)** shows the *projected* velocities $v \sin i$ as would be inferred from the Doppler shift.

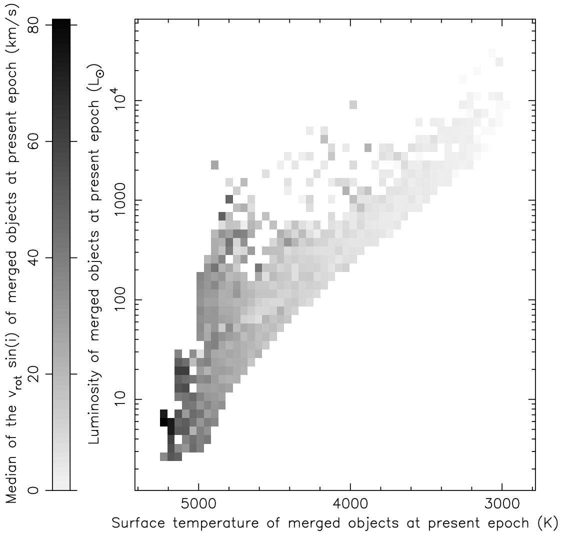

Figure 3. Two-dimensional histogram of the projected equatorial rotational velocities, $v \sin i$ (in km/s), of the merged objects in our standard model, overlaid on an HRD.

r_e, respectively) as

$$e = \sqrt{1 - \left(\frac{r_\mathrm{p}}{r_\mathrm{e}}\right)^2}. \qquad (6)$$

We note that for a constant density, this function resembles a straight line for the regime of our interest ($e < 0.85$) and we use a simple least-squares method to find that the best slope for a line through the origin ($e = 0, \omega = 0$) to describe this part of the function (to an accuracy of 2.5% or better) is 0.53. This allows us to derive an approximation for the oblateness as a function of the angular frequency and the density

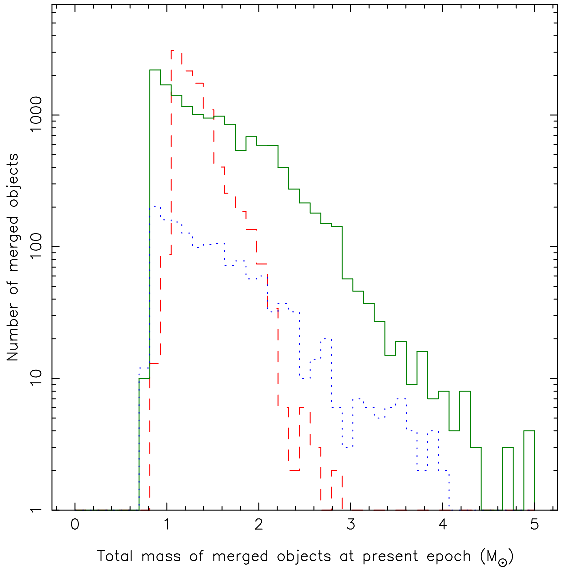

Figure 4. Distribution of the total masses in our standard model population of present-day merged objects for three sub-populations: RGB stars (dashed curve), HB stars (solid curve) and AGB stars (dotted curve).

$$e \approx \frac{\omega}{0.53\,\sqrt{2\pi G\rho}} = \frac{0.75\,\omega}{\sqrt{G\rho}}; \quad e < 0.85 \qquad (7)$$

and to compute the oblateness for each of the merger products in our standard population.

Figure 8a shows the distribution of the oblateness of the stars in our present-day populations of RGB, HB and AGB stars. We find that for most stars the eccentricity is larger than 0.1 and should be observable if the

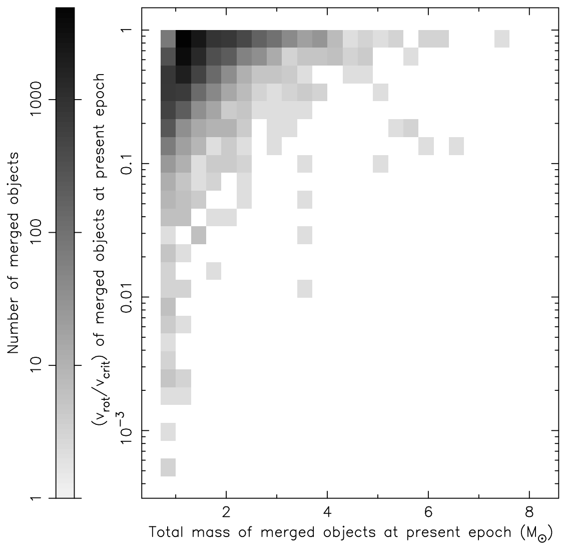

Figure 5. Two-dimensional distribution of the rotational velocities and total masses in our standard model population of present-day merged objects. The grey scale represents the total number of merged objects per two-dimensional bin. As in Fig. 1, the rotational velocities are given as a fraction of the assumed critical rotational velocity.

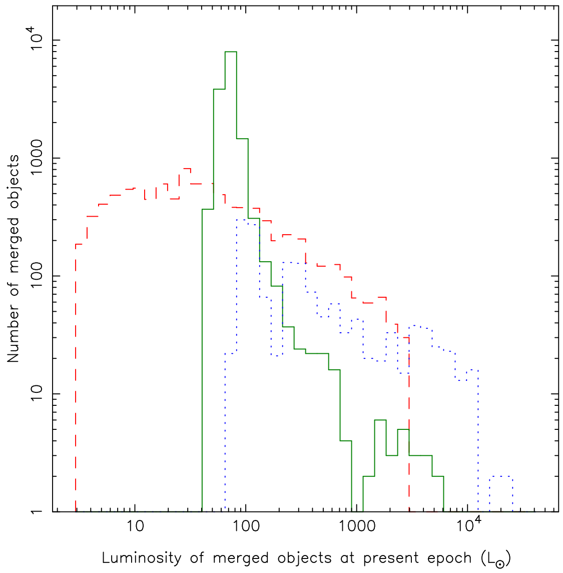

Figure 6. Distribution of the luminosities in our standard model population of present-day merged objects for three sub-populations: RGB stars (dashed curve), HB stars (solid curve) and AGB stars (dotted curve).

star is not too distant (see *e.g.* Zhao et al. 2009). All three distributions peak at the maximum value of the oblateness ($e \approx 0.5$). While the histograms for the RGB and HB drop off rapidly towards smaller oblateness, the histogram for AGB stars does so less steeply and there are a small number of AGB stars with a small eccentricity ($e < 0.01$). Figure 8b displays the distribution of eccentricities on an HRD and shows that the most deformed stars are at the base of the red-giant branch, the HB and the lower AGB, while the most expanded giants have shapes that are closer to spherical. The distributions of eccentricities follow those of $\log(v_{\rm rot}/v_{\rm crit})$ in Figs. 1 and 7b. We stress that our model of a MacLaurin spheroid for the shape of these stars has limited validity and the fit in Eq. 7 depends on our choice of β. For example, if $\beta = 1$, this fit, and the assumption of MacLaurin spheroids, would yield physically meaningless results. Consequently, our use of MacLaurin spheroids is meant to provide rough order-of-magnitude estimates and trends, not precise values.

3.2. *Dependence upon input parameters*

In addition to our standard model, we investigated the dependence of our results on three uncertain input parameters: the CE efficiency parameter, $\alpha_{\rm CE}$, the initial mass ratio distribution in ZAMS binaries, $g(q)$, and the assumed critical rotational velocity at which mass is lost, $v_{\rm crit}$ (see item 1 of § 2.2.1). Uncertainties in the first two parameters plague the majority of population synthesis calculations involving close binary systems, while uncertainty in the third parameter is specific to the present calculations. We calculated model populations for two other choices of each parameter and have listed the parameter choices for each model in Table 1. In all cases, only one parameter was varied at a time, keeping the other two at their default values.

Selected results from these non-standard models for the three sub-populations discussed in § 3.1 and for the total population are shown in Table 2. We find that, with a few notable exceptions, varying these input parameters has relatively little effect on the overall characteristics of the present-day population of merged objects. For example, the fraction of the population that is rotating slowly ($v_{\rm rot} \leq 0.1\, v_{\rm crit}$) is uniformly small for all choices of input parameters: in the RGB and HB sub-populations, this fraction is either zero or so small as not to be statistically significant; in the AGB sub-population, this fraction is 7 – 9%; and for the total population, this fraction is barely significant (< 1%). Further, with the exception of the $v_{\rm crit} = v_{\rm br}$ model, the present-day median mass in the total population varies from $1.20\, M_\odot$ to $1.29\, M_\odot$ and the variation within a given sub-population is only slightly greater. The median mass in the $v_{\rm crit} = v_{\rm br}$ model is systematically greater than the others because the merged object can assimilate more angular momentum (and hence mass) during the merger before it reaches its critical rotation velocity (see assumption 2 in § 2.2.1). As expected, the median projected rotational velocity, $v \sin i$, is strongly correlated with our assumed choice for $v_{\rm crit}$; a larger value for $v_{\rm crit}$ allows a higher median projected rotational velocity. There is somewhat greater variation among the models in the fraction of present-day merged objects rotating at $v_{\rm crit}$. In the total population, this fraction varies by a factor of 2, from 0.13 for the $v_{\rm crit} = v_{\rm br}$ model to 0.27 for the $\alpha_{\rm CE} = 0.1$ model, compared with 0.19 for our standard model. The same trend is found in the RGB and HB sub-populations. Virtually none of the AGB stars are rotating critically, because of the large rotational inertia of the envelopes in these stars.

The largest variation within the present-day population caused by changing the input parameters is found in the total number of merged objects. For the total population and within a given sub-population, the total number of present-day merged objects varies by roughly 20% to 50%, with the smallest number of objects found in the $v_{\rm crit} = v_{\rm br}$ model population (24,414 stars, or 0.24% of the input population) and the largest (32,882 stars, or

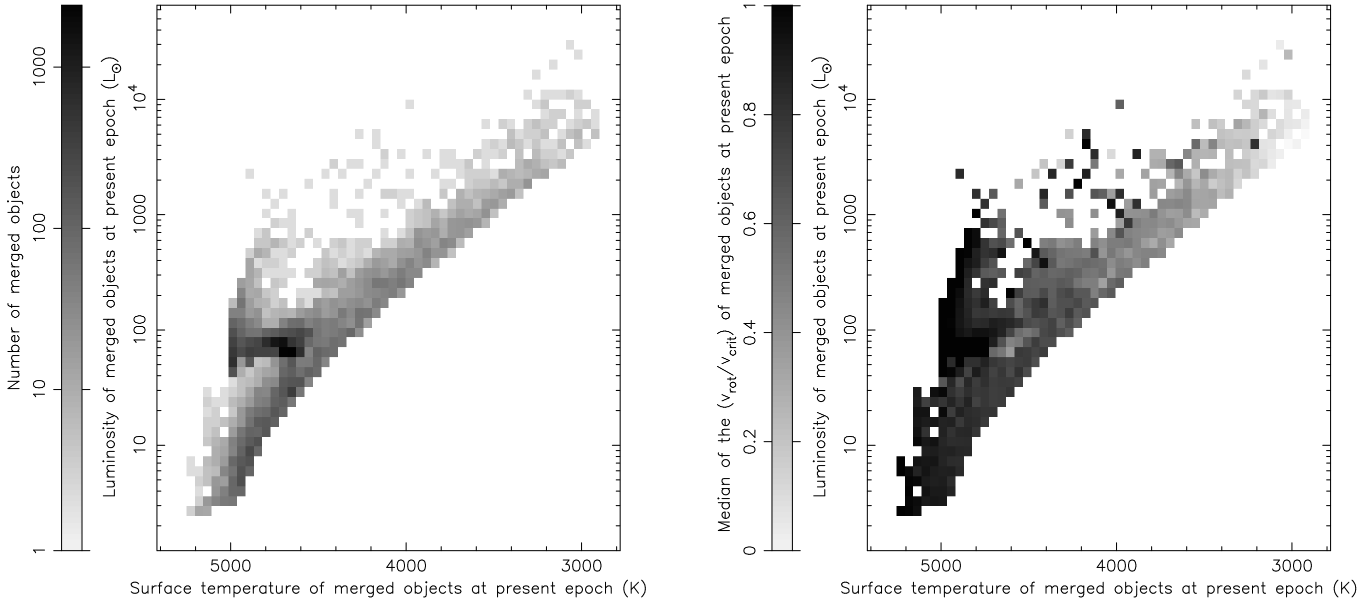

Figure 7. Two-dimensional distribution of the luminosities and effective temperatures in our standard model population of present-day merged objects. In the left-hand panel **(a)**, the grey scale represents the total number of merged objects per two-dimensional bin (pixel). The lightest grey scale, which represents a bin with one star, is easily distinguished from the white background. In the right-hand panel **(b)**, the grey scale represents the median of the distribution of rotational velocities (as a fraction of $v_{\rm crit}$) per pixel. Temperature increases to the left on the horizontal axis to facilitate comparison with observational HR diagrams.

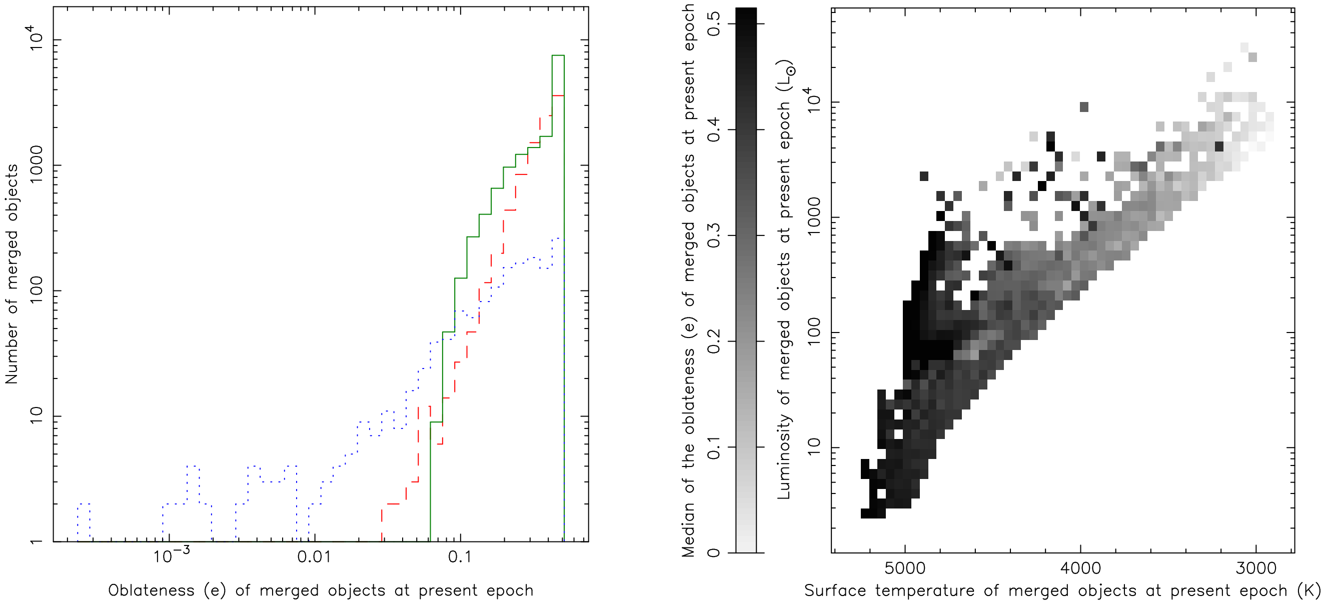

Figure 8. Distributions of the oblateness e (see Eq. 6) in our model population of present-day merged objects. Left-hand panel **(a)**: histograms for the sub-populations of RGB stars (dashed line), HB stars (solid line) and AGB stars (dotted line). Right-hand panel **(b)**: two-dimensional distribution of the oblateness on an HRD. The stars at the base of the RGB are most deformed, whereas very large giants are nearly spherical.

0.33% of the input population) in the $\alpha_{\rm CE} = 0.1$ model (except for RGB stars, where the largest number is found in the $v_{\rm crit} = 0.1\,v_{\rm br}$ model). Reducing the value of $\alpha_{\rm CE}$ results in a less efficient transfer of orbital energy to the CE during spiral-in, thereby increasing the number of systems that merge during the CE phase. This increase in the number of CE mergers results in a larger number of present-day merged objects. As one might expect, varying $v_{\rm crit}$ has very little effect on the total number of present-day merged objects.

Column 8 of Table 2 lists the mass that is not assimilated from the binary during merger, $M_{\rm rej}$, and column 9 lists this mass as a fraction of the total mass of the binary at the beginning of the CE phase. We find that varying the choice of $\alpha_{\rm CE}$ has essentially no effect on the amount of mass rejected during merger. Increasing $v_{\rm crit}$ decreases $M_{\rm rej}$, which is as expected since for larger values of $v_{\rm crit}$, the merged object can assimilate a greater fraction of the mass of the binary before it starts to spin critically. Perhaps surprisingly at first, varying $g(q)$ has the strongest effect on the value of $M_{\rm rej}$. However, this is simply because $g(q)$ determines the ZAMS distribution of secondary masses. For $g(q) = q$, equal mass ZAMS binaries are strongly favored, resulting in systematically larger secondary masses than in our standard model. Conversely, for $g(q) = q^{-0.9}$, extreme mass ratio ZAMS binaries are strongly favored, resulting in systematically smaller secondary masses than in our standard model. Consequently, for $g(q) = q$, $M_{\rm rej}$ is larger than in our standard model because the secondaries are more massive. On the other hand, for $g(q) = q^{-0.9}$, $M_{\rm rej}$ is smaller than in our standard model because the secondaries are less massive.

The last column in Table 2 lists the fraction of mass lost by the merged objects between the moment immediately after merger and the present epoch. This fraction is vanishingly small for present-day RGB stars, but is ∼12% for objects that are currently on the HB and AGB, indicating that this post-merger mass loss occurs predominantly near the moment of core helium ignition. Two factors contribute to this mass loss: (1) normal stellar winds near the tip of the RGB *prior* to helium ignition and (2) rotationally-enhanced mass loss during contraction to the HB *after* helium ignition. A typical RGB star spends most of its time on the lower part of the RGB without much mass loss. Then, in a relatively short time, the star evolves to the tip of the RGB, where mass loss becomes significant. For example, in the $1.3\,M_\odot$ stellar model in our grid, $\sim 0.2\,M_\odot$ is lost on the RGB, with 90% of this mass lost in the last 4% of the time spent on the RGB. While wind mass loss on the RGB is present whether or not merger occurs, we find that for a substantial number of objects that merge on the RGB, additional mass loss occurs during the star's contraction after helium ignition. Especially in stars that undergo a helium flash, where the decrease in stellar radius is large, the rotational velocity of the merged object becomes critical as the star contracts to the HB. A period of enhanced mass loss ensues, until the star has lost a sufficient amount of angular momentum for the rotational velocity to drop below critical. While we do not distinguish between these two contributions in column 10 of Table 2, we note that the post-merger mass loss is lower in the $v_{\rm crit} = v_{\rm br}$ model since the larger value for $v_{\rm crit}$ allows the stars to reach larger rotational velocities before they start to experience rotationally-enhanced mass loss during contraction to the HB.

3.3. *Comparison with single stars*

In this section, we compare our present-day model population of merged objects to a model population of normal present-day single stars. We generated 10^7 single ZAMS stars, drawing their initial masses from the same IMF that was used for the merged objects, and determined the structure and evolution of these stars using the same grid of stellar models that was used to generate the merged object population (see § 2.1). We consider only those present-day single stars that are on the RGB, HB or AGB for this comparison. In Fig. 9, we show the present-day distribution of rotational velocities for our single stars in each of these evolutionary phases. As before, the rotational velocity for a given star is shown as a fraction of the critical rotational velocity for that star, defined as in our standard model ($v_{\rm crit} = \frac{1}{3}\,v_{\rm br}$). The present-day rotational velocities for single stars were calculated using the following expression for rotational velocities in ZAMS stars as a function of mass (Hurley et al. 2000, Eq. 107),

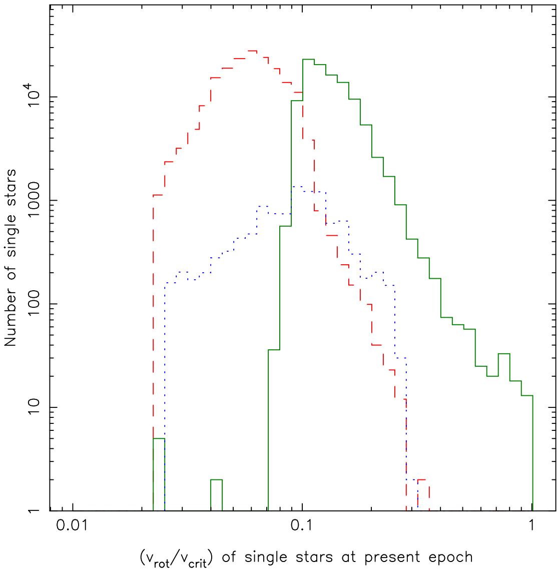

Figure 9. Distribution of the rotational velocities in a comparison model of normal present-day single stars constructed from the same grid of stellar evolution models used for the merged population. As in the corresponding plot for the merged population (Fig. 1), the rotational velocities are given as a fraction of the assumed critical rotational velocity and the distribution is separated into three sub-populations: RGB stars (dashed curve), HB stars (solid curve) and AGB stars (dotted curve).

$$v_{\rm rot,ZAMS} = \frac{330\,M^{3.3}}{15.0 + M^{3.45}}\ {\rm km\,sec^{-1}}, \qquad (8)$$

conserving angular momentum up to the base of the RGB, and then accounting for angular momentum loss from the star via stellar winds throughout the remainder of the evolution. Once again, angular momentum loss due to magnetic braking was not incorporated in the evolution.

Comparison of Fig. 9 with the corresponding plot for the merged objects (Fig. 1) reveals a striking contrast in the rotational velocities for the two populations. The peak rotational velocity for each sub-population of merged objects is approximately an order of magnitude higher than the corresponding peak rotational velocity for normal single stars. This difference can be seen even more clearly in Fig. 10, which shows the distribution of rotational velocities for the total populations of merged objects and single stars. Not only are the peak rotational velocities markedly different, but the overlap between the two distributions is relatively small. Consequently, observational determinations of rotational velocities in RGB, HB and AGB stars may be expected to provide an important diagnostic in determining which stars are the result of a CE merger.

In Fig. 11, we show the present-day distribution of masses for RGB, HB and AGB stars in our single star population. Comparison of this plot with the corresponding plot for the merged objects (Fig. 4) reveals that the

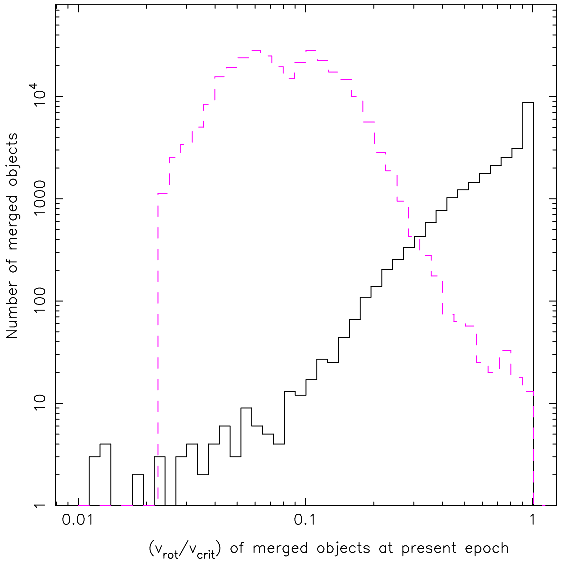

Figure 10. Distribution of the rotational velocities in our model population of present-day merged objects (solid curve) and in a corresponding present-day population of normal single stars (dashed curve) calculated using the same grid of stellar evolution models. The solid curve represents the sum of the combined sub-populations of RGB, HB and AGB stars shown in Fig. 1 and the dashed curve represents the sum of the combined sub-populations of RGB, HB and AGB stars shown in Fig. 9. As in those two figures, the rotational velocities here are given as a fraction of the assumed critical rotational velocity.

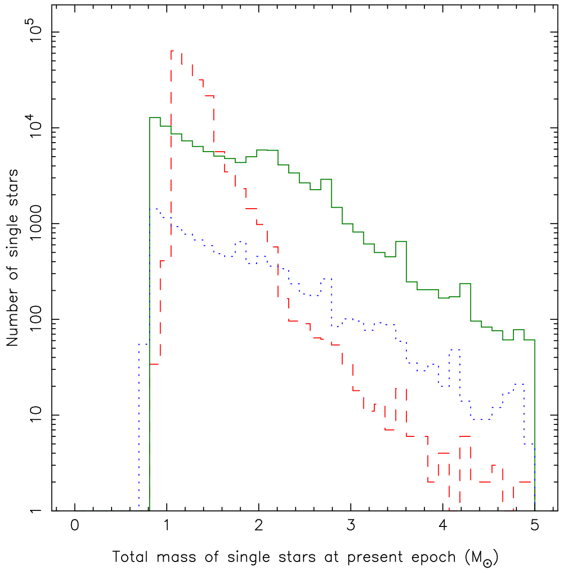

Figure 11. Distribution of the total masses in a comparison model of normal present-day single stars constructed from the same grid of stellar evolution models used for the merged population. As in the corresponding plot for the merged population (Fig. 4), the distribution is separated into three sub-populations: RGB stars (dashed curve), HB stars (solid curve) and AGB stars (dotted curve).

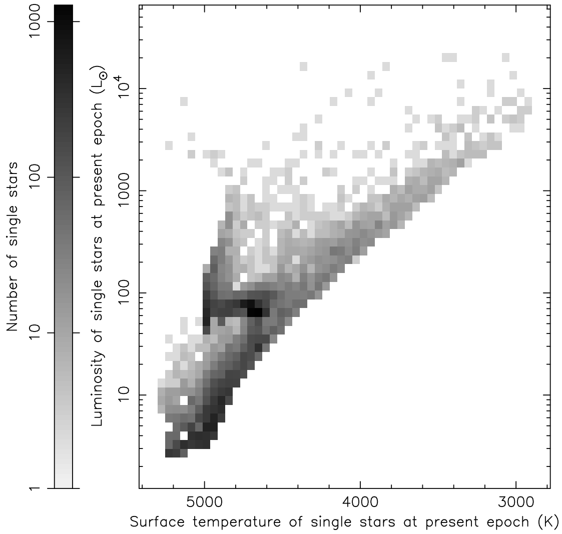

Figure 12. Two-dimensional distribution of the luminosities and effective temperatures in a comparison model of normal present-day single stars constructed from the same grid of stellar evolution models used for the merged population. The grey scale represents the total number of merged objects per two-dimensional bin. Temperature increases to the left on the horizontal axis to facilitate comparison with observational HR diagrams.

merged objects have a slightly steeper drop-off towards higher masses than the single stars, which is due to rotationally-enhanced mass loss from many of the merger products during their post-merger evolution. However, as can be seen by comparing the median present-day masses listed in Table 2 for the total population in our standard model and the single-star population, this difference is small ($0.05\,M_\odot$). On the other hand, the relative percentages of RGB, HB and AGB stars are quite different for the two populations. While the merged object population consists of 37% RGB stars, 57% HB stars and 5.7% AGB stars for our standard model, the respective percentages for the normal single star population are 61%, 36% and 3.6%. The ratios of these percentages are 0.61, 1.6 and 1.6, respectively, which suggests that this is caused by a shift in numbers between the pre- and post-helium-ignition phases. In other words, in a present-day population of merged objects on the RGB, HB and AGB, the majority of stars have ignited helium, while in a corresponding normal single-star population consisting of the same three sub-populations, the majority of stars have not yet ignited helium. This is understandable since for the merged objects, we only consider a star *after* it has merged, which is in 99.9% of the cases somewhere on the RGB (see § 3.1.1). Hence, its subsequent evolution as a merged object consists of only *part* of the RGB, but the *full* HB and AGB.

In Fig. 12, we show a present-day, binned, theoretical HR diagram for our normal single-star population. Comparison of Fig. 12 with the corresponding plot for merged objects (Fig. 7a) indicates little difference between the two plots. This apparent similarity results from the use of our grid of normal single-star models to calculate the structure and evolution of the merged objects. This approximation was necessary because of the lack of suitable stellar structure and evolution models for objects that merge during the CE phase. The degree of error introduced in our predicted luminosities and effective temperatures by using non-rotating stellar models is not clear.

4. DISCUSSION

We have shown that a distinguishing characteristic feature of a merged stellar population is the high rotational velocity in comparison with a single-star population.

Specifically, rapid rotation in the merged population is expected for a fraction of stars in their giant phase or horizontal-branch phase of evolution. Among observed RGB stars, rapid rotators[6] account for 1% to 6% of the red giant population, depending on the specific observational sample (see Carlberg, Majewski, & Arras 2009, and references therein). Fig. 2 shows that ∼70% of the projected rotational velocities in our standard merged object population are greater than $10\,\mathrm{km\,s^{-1}}$. Combining this with the number of RGB stars in our merged object and normal single star model populations from Table 2, and assuming a ZAMS binary fraction of 0.5, we estimate the fraction of rapid rotators in the RGB population due to CE mergers is $\sim 3.4\%$. We note that this estimate neglects RGB stars in binaries whose orbits are wide enough to avoid mass transfer, since such binaries are excluded from our population of merged objects. Inclusion of these binaries increases the overall number of RGB stars, which would lower our estimate. However, it is also true that tidal interactions between the RGB star and its lower-mass companion can still spin up the giant star in some of these detached binaries. Even though such a system retains its binarity, the presence of the companion may be masked by the much brighter RGB star and the system could be misidentified observationally as a solitary RGB rapid rotator. At the moment, it is uncertain to what extent such misidentifications are present in the observational estimates above. We also point out that Carlberg, Majewski, & Arras (2009) estimate that rapid rotators produced by the ingestion of planets by RGB stars, which we do not consider, can account for $\sim 0.6\%$ of the RGB population.

The subsequent evolution of rapidly rotating RGB stars can lead to the production of rapidly rotating HB stars as a result of the contraction of stars from the tip of the RGB to the HB when helium is ignited in the core (see § 3). Although we find theoretical evidence for the rapid rotation of stars in a clump on the red portion of the HB in our HR diagram (see Fig. 7), observational evidence for rapid rotation among red HB field stars is lacking (e.g., Behr 2003; de Medeiros 2004). However, in a sample of 45 HB field stars, Behr (2003) found evidence for rapid rotation ($v \sin i \gtrsim 30\,\mathrm{km\,s^{-1}}$) in several blue HB field stars ($7500\,\mathrm{K} < T < 11{,}500\,\mathrm{K}$). He suggests that the underlying distribution of actual rotational velocities in blue HB field stars may be bimodal, consisting of a slow population ($v \sin i \sim 10$ km s^{-1}) and a fast population ($v \sin i \sim 30$ km s^{-1}), similar to the bimodal distribution found in many globular clusters. If a larger sample of HB field stars confirms the possibility of a bimodal distribution in rotational velocities, the fast-rotating population may result from the mergers studied in this paper. As already pointed out by Politano et al. (2008), the merged population of very rapidly rotating HB stars may evolve under the action of enhanced stellar wind mass loss due to the reduction of surface gravity associated with centrifugal effects. As a result, some very rapidly rotating HB stars may lose a significant fraction of their envelope, which would cause both a reduction in the rotation rate of the star because of the associated angular momentum loss, and a blueward movement in the HR diagram. Such stars may contribute to the rapid rotation of blue HB stars in the field found by Behr (2003) and, if sufficient mass is lost, provide an evolutionary channel for the formation of single sdB stars. Politano et al. (2008) predict a spectrum of masses ranging from 0.32 to $\sim 0.7\,M_\odot$ with a strong peak between 0.47 and $0.54\,M_\odot$. This is consistent with the small number of observationally determined masses for single sdB stars, the majority of which have masses between 0.46 and $0.54\,M_\odot$, but can be as small as $0.39\,M_\odot$ (PG 0911+456; Randall et al. 2007). We further note that, although our models have solar metallicity, if similar rapid rotation and subsequent mass loss on the HB is found for merger models with lower metallicities, this may be relevant to the extended HB morphologies found in globular clusters (e.g., Moni Biden et al. 2008).

Another class of stars that possibly may result from a merger during CE evolution are FK Comae stars. These stars are rapidly rotating giants with $v \sin i \sim 100\,\mathrm{km\,s^{-1}}$ and spectral types G and K (Bopp & Stencel 1981). An origin involving the evolution of a rapidly rotating single MS star is not a viable one, since the progenitors of FK Comae stars would have rapid rotation and be chromospherically active, whereas none have been discovered. On the other hand, the coalescence of evolved contact binaries (see Webbink 1976) remains as a viable evolutionary scenario, and we suggest that the merger of non-corotating CE binaries may also contribute to this population. We note, however, that our current model population does not contain merged objects of the correct spectral type, although this may be due to our use of non-rotating stellar models for these objects. Incorporation of stellar models that include rotation would be especially important in determining the viability of the merger scenario for FK Comae stars.

As a consequence of the merger process, it is likely that there exists a nonspherical distribution of circumstellar matter surrounding the remnant, either resulting from matter which is not accreted nor ejected from the system during merger or from an enhanced mass-loss phase from the equatorial region of the rapidly rotating star. In the former case, there may exist a short phase (depending on the mass in the circumstellar envelope) where the interaction of the stellar wind with this disk structure can lead to the development of a bipolar outflow (where outflow in the equatorial region is impeded by the presence of the circumstellar disk). Furthermore, it is likely that the mass-loss history of the remnant following the merger event would be variable, and that the circumstellar matter distribution would reflect its integrated history since the merger event. For example, such a temporal history may be responsible for the formation of a torus-like structure embedded within a continuous outflow, the existence of which has been postulated for the shaping of planetary nebulae in the generalized interacting-stellar-winds model (see Kwok 1982; Kahn & West 1985), and which has been inferred from HST observations of the proto-planetary nebula IRAS 17106-3046 (see Kwok et al. 2000).

Such structures are of interest, especially for AGB stars, since observational evidence of axisymmetric circumstellar envelopes in post-AGB stars and preplanetary nebulae exists (*e.g.*, Sahai & Trauger 1998). The mass loss in AGB stars is generally spherically symmetric (*e.g.*, Bowers et al. 1983; Sahai & Bieging 1993; Olofsson 2004), although observational evidence of asymmetrical structure exists in the AGB star V Hya (see Hirano et al. 2004). Given this state of affairs, the evolutionary state of stars leading to the transition from a spherical circumstellar envelope to a nonspherical morphology is of great interest both theoretically and observationally. The results of our study suggest that the frequency of occurrence of nonspherical circumstellar-envelope structures resulting from the merger of the components of a binary system during CE evolution is not high (at best $\sim 10\%$, assuming all merged AGB stars contain asymmetric envelopes, although it is not clear whether mergers between AGB stars and planets would lead to asymmetric envelope structures as well). Hence, if the nonspherical structures are not uncommon and a result of binary star interactions, then they may reflect the population of detached systems in wide binaries (*e.g.*, Huggins et al. 2009) or those remnant binary systems that have survived the CE phase resulting in short orbital periods. An extension of our population synthesis study to examine the orbital properties of the detached systems and the effect of gravitational focusing on the shape of the AGB envelopes will be the subject of a future investigation.

---

[6] We follow the literature in defining rapid rotators as those RGB stars with $v \sin i \geq 10\,\mathrm{km\,s^{-1}}$.

The effect of rotation in the deeper interior layers of the merger remnant may affect the composition of matter in the surface layers if rotationally induced mixing of matter develops. In such cases, the elemental abundances in the surface layers may show anomalies compared to those of normal single stars, as matter may be mixed from the outer radiative regions of the hydrogen burning shell to the base of the convection zone and, hence, to the surface. The changes in the abundances, however, sensitively depend on details regarding the magnitude of the diffusion coefficient and the depth of the mixing (see for example, Palacios et al. 2006).

Of particular interest with regard to the nucleosynthetic anomalies at stellar surfaces are the Li-rich stars. These stars are located near the red-giant bump region at luminosities of $\sim 60\,L_\odot$, and in the early AGB phase at luminosities of $\sim 600\,L_\odot$ (see Reddy & Lambert 2005; Kumar & Reddy 2009). The stars near the red-giant bump may have masses of the order of $\sim 1-2.4\,M_\odot$, based on comparison of their luminosities and effective temperatures with red-giant evolutionary tracks. A comprehensive discussion of the theoretical models (including the merger of a red giant with a Jupiter mass type planet), involving the conversion of ^{3}He to ^{7}Be, the formation of ^{7}Li via electron capture (Cameron & Fowler 1971), and mixing associated with an enhanced diffusion coefficient (presumably a result of rapid rotation), is given in Denissenkov & Herwig (2004). If the effectiveness of the rotation-induced mixing is related to the location of the bottom of the surface convection zone relative to the hydrogen burning shell, then such mixing may take place in stars above the base of the giant branch, as the mass lying between the base of the convection zone and the outer edge of the hydrogen burning shell decreases with increasing evolutionary state. Given that the proportion of Li-rich giants among rapid rotators ($v \sin i > 8\,\mathrm{km\,s^{-1}}$) is $\sim 50\%$ (see Denissenkov & Pinsonneault 2008), which is considerably greater than the $\sim 2\%$ of Li-rich stars among slowly rotating stars ($v \sin i < 1\,\mathrm{km\,s^{-1}}$), it is suggestive that rapid rotation may play an important role in forming a significant fraction of the Li-rich giant population.

An additional observation suggesting a possible connection between Li-rich stars and the merged remnants envisioned here is the relation between the Li abundance and the far-infrared excess in these stars. In particular, de la Reza et al. (1996) suggest that an enhanced mass loss event may accompany the Li-enrichment phase. The mass loss resulting from the phase is expected to be significantly greater (about 2 orders of magnitude) than that for normal Li-poor giants. It should be noted that the far-infrared emission may have its origin in a disk-like configuration resulting from the merging process rather than an expanding dust shell.

5. SUMMARY AND CONCLUSIONS

The population of binary star systems consisting of an RGB or AGB star with a lower-mass companion that merge during CE evolution has been explored via a population synthesis technique. Using a suite of 116 evolution tracks for single stars and including the rotational evolution of the primary components, we have evolved 10^7 ZAMS binary systems. The characteristic properties of the merger remnants have been examined as a function of uncertain population synthesis input parameters, such as the initial mass-ratio distribution of the binary population and the efficiency for mass ejection in the CE phase, as well as the critical rotational velocity at which enhanced mass loss occurs for the merged object. Using simplified prescriptions for the binary interaction during the CE stage and for the rotational and nuclear evolution of the merger remnant, we find that the present-day merged population is primarily distinguished by its high rotation speed. For the total merged population, the median projected rotational velocity is $16.2\,\mathrm{km\,s^{-1}}$, in contrast to $2.3\,\mathrm{km\,s^{-1}}$ for a theoretical population of normal single stars calculated using the same stellar models and initial mass function. This relative difference is also reflected in individual sub-populations of merged objects (see below), whose peak rotational velocities are an order of magnitude higher than those in corresponding sub-populations of normal single stars.

In our present-day model population of merged objects, we include only those objects that are on RGB, HB or AGB. We find that these objects constitute between 0.24% and 0.33% of the initial population of 10^7 ZAMS binaries, depending upon the values chosen for the input parameters. In addition, we find that HB stars are the most populous (57%), followed by RGB stars (37%) and then AGB stars (6%). The luminosities of these subgroups overlap and lie in the range of $\sim 10-100\,L_\odot$, with the majority of the present-day merged population consisting of HB stars with luminosities of $\sim 60\,L_\odot$, virtually indistinguishable from their present-day, normal single-star counterparts with the exception of their high rotation speed. The masses characteristic of the total population in our standard model are $\lesssim 2\,M_\odot$, with median masses for RGB ($1.20\,M_\odot$), HB ($1.35\,M_\odot$) and AGB ($1.34\,M_\odot$) stars that do not significantly differ from those for normal single stars on the RGB, but are clearly lower than those for single stars on the HB and AGB. The median mass of the total population is about $0.05\,M_\odot$ higher for our standard merger population than for a normal single-star population, which may seem to contradict the results per sub-population, but can be explained by the different RGB versus HB ratios between merged objects and normal single stars (see § 3.3). These quantitative features of the present-day merged population are found to be relatively insensitive to the population synthesis input parameters.

The results of our population synthesis study have been discussed in terms of possible observational counterparts either directly involving the high rotational velocity of the component or indirectly, via the effect of rotation on the amount and distribution of circumstellar matter. Additional probes potentially indicating the occurrence of such interactions could be provided by compositional signatures on the stellar surface. As a specific application of our CE merger model, we have considered the possibility that rotationally enhanced mass loss may be sufficient to significantly deplete low- or intermediate-mass hydrogen-rich envelopes of rapidly rotating HB stars to the extent that their effective temperatures are increased sufficiently to produce sdB stars. Such a merger scenario can provide an additional evolutionary channel for the formation of single sdB stars (Soker & Harpaz 2000, 2007; Politano et al. 2008), complementary to the double helium-WD merger channel proposed earlier by Han et al. (2003).

Indirect effects associated with the merger and rapid rotation, coupled with the evolution of the merged object to its later phases, can lead to deviations from spherical symmetry in the distribution of circumstellar matter. Such structures can be potentially probed via their emission in the radio (*e.g.*, Hirano et al. 2004) or infrared wavelength region, or via the scattering of optical light (*e.g.*, Mauron & Huggins 2006). These structures may result from inherent asymmetries present in the merger process itself, or result after the merger has already occurred, reflecting asymmetric mass loss from the stellar surface or the interaction of a spherically symmetric stellar wind with a nonspherical distribution of circumstellar matter. Additional observational effects may be a consequence of rotation in the deep interior, possibly resulting from rotationally induced compositional mixing leading to the production of nucleosynthetic anomalies at the stellar surface. In this regard, the merger scenario may provide an additional evolutionary channel for producing Li-rich RGB stars.

To gain insight into the outcome of the merger scenario, our investigation has been primarily exploratory in nature. As a result, the study has been based on a number of simplifying assumptions. Foremost among them is the treatment of the structure and evolution of a merged object as equivalent to a single, non-rotating star of the same total mass and core mass. The binary interaction involving the evolution into and during the CE phase is also uncertain, as the efficiency of mass ejection has been assumed to be a constant, independent of evolutionary phase. Mass loss prior to and after the CE phase has been based on rates inferred for normal single stars, which are likely to have much smaller rotational velocities. Finally, it is likely that the mass loss via a stellar wind, and hence angular momentum loss from the system, would be affected by the spin-orbit tidal coupling and magnetic braking.

To improve on the numerical modeling, future theoretical work is indicated, especially in including neglected effects. For example, the use of a grid of stellar models resulting from the merger process (see for example, Glebbeek & Pols 2008) would be particularly illuminating, not only in describing the structure and properties of the merged remnant, but also in determining their evolutionary characteristics as a function of age. This would be most useful for our large population of merged objects on the RGB and HB. Our work also provides valuable guidance by better defining the region of parameter space where detailed multi-dimensional hydrodynamical calculations are highly desirable. We find that mergers during CE evolution likely happen in binaries characterized by primaries with masses of $\sim 1-2\,M_\odot$ that fill their Roche lobes on the lower half of the RGB at orbital periods between ~ 1 and 30 days. Our study also points to the phases of evolution where hydrodynamical or magnetohydrodynamical calculations are needed to explore the influence of rotation and/or magnetic fields in the mixing of matter and angular momentum from the the deep interior (e.g., regions that have undergone nuclear processing) to the stellar surface. Incorporation of mixing prescriptions, based on the above studies, into evolutionary calculations of a merged remnant could provide quantitative estimates of the influence of rotation on the surface composition. Of special interest would be numerical modeling of the rotating remnant during a helium flash, as it may provide a compositional probe of the possible mixing of matter between the helium core and hydrogen-rich envelope for stars that are now on the HB. Finally, an extension of our models to examine the properties of binaries that merge in the MS phase of evolution is of interest, as they may have applications to highly luminous transient events, perhaps similar to that observed in V 838 Mon (see for example, Soker & Tylenda 2006).

In addition to the fundamental theoretical work, future observational programs aimed at detecting the effects of rapid rotation using ground-based optical interferometers could be fruitful in the determination of the shapes of giant stars, where temperature variations of the surface may be probed (*e.g.*, Zhao et al. 2009). A program of highly accurate photometric studies can be considered, enabling one to detect differences in luminosity and colors of rapidly rotating stars in comparison to their single-star counterparts. For example, observational evidence exists that magnetically-active, rapidly rotating, low-mass MS stars in eclipsing binaries are characterized by effective temperatures that are lower than, radii that are larger than, and luminosities that are approximately equal to those predicted from corresponding theoretical stellar models of the same mass (*e.g.*, Torres et al. 2009). The same stellar models satisfactorily match observations of similar-mass stars that are rotating more slowly in wide binary orbits. Torres et al. (2006), López-Morales (2007), Morales et al. (2008) and others have shown that the source of these differences is the magnetic activity in the rapidly rotating stars. Whether the radii, effective temperatures and luminosities in rapidly rotating giant or HB stars would be similarly affected is an interesting and unresolved question. Finally, studies on the asymmetries in the circumstellar envelope of stars in the AGB phase with upcoming facilities (*e.g.*, ALMA) will be especially useful in providing constraints on the stellar evolutionary phases where asymmetries develop. Such studies will be very important for distinguishing the contributions of the merged population from the existing binary population, thereby potentially providing further constraints on uncertain population synthesis input parameters and possible shaping mechanisms for the origin of the asymmetries seen to be prevalent in the post-AGB and proto-planetary nebula phase.

We warmly thank P.P. Eggleton for making his binary-evolution code available to us. M.P. acknowledges funding from the Wisconsin Space Grant Consortium and NSF grant AST-0607111, sub-award 1-2008, to Marquette University. MvdS acknowledges support from NSF CAREER Award AST-0449558 to Northwestern University and a CITA National Fellowship to the University of Alberta. R.T. and B.W. acknowledge support from NSF AST-0703950 and NASA BEFS NNG06GH87G, respectively, to Northwestern University. Lastly, we thank the referee, Dr. Evert Glebbeek, for a thorough reading of our manuscript and many useful comments that improved the paper.

REFERENCES

Abt, H.A. 1983, ARA&A, 21, 343
Baraffe, I., Chabrier, G., Allard, F., & Hauschildt, P. 1998, A&A, 337, 403
Baraffe et al. 2003, A&A, 402, 701
Behr, B. B. 2003, ApJS, 149, 101
Bopp, B. W., & Stencel, R. E. 1981, ApJ, 247, L131
Bowers, B. F, Johnston, K. J., & Spencer J. H. 1983, ApJ, 274, 733
Busso et al. 2007, A&A, 47, 105
Cameron, A. G. W., & Fowler, W. A. 1971, ApJ, 164, 111
Carlberg, J.K., Majewski, S.R., & Arras, P. 2009, ApJ, 700, 832
Catelan, M. 2007, in New Quests in Stellar Astrophysics II: The Ultraviolet Properties of Evolved Stellar Populations, ed. M. Chavez, E. Bertone, D. Rosa-Gonzalez, & L. H. Rodriguez-Merino, (New York: Springer), 175
Chabrier, G. & Baraffe, I. 1997, A&A, 327, 1039
Chabrier, G. & Baraffe, I. 2000, ARA&A, 38, 337
Chabrier, G., Baraffe, I., Allard, F., & Hauschildt, P.H. 2000, ApJ, 542, 464
Darwin, G.H. 1879, Proc. Roy. Soc., 29, 168
de Jager, C., Nieuwenhuijzen, H., & van der Hucht, K. A. 1988, A&AS, 72, 259
De la Reza, R., Drake, N. A., & Da Silva, L. 1996, ApJ, 456, L115
de Medeiros, J. R. 2004, in Stellar Rotation, IAU Symposium No. 215, ed. A. Maeder & P. Eenens (San Francisco: Astronomical Society of the Pacific), p. 144
Denissenkov, P. A., & Herwig F. 2004, ApJ, 612, 1081
Denissenkov, P. A., & Pinsonneault, M. 2008, ApJ, 684, 626
Dorman, B., Rood, R.T., & O'Connell, R.W. 1993, ApJ, 419, 596
Duquennoy, A., & Mayor, M. 1991, A&A, 248, 485
Eggleton, P. P. 1971, MNRAS, 151, 351
Eggleton, P. P. 1972, MNRAS, 156, 361
Fryer, C. L., & Woosley, S. E. 1998, ApJ, 502, L9
Fryer, C. L., & Heger, A. 2005, ApJ, 623, 302
Glebbeek, E., & Pols, O. R. 2008, A&A, 488, 1017
Goldberg, D., Mazeh, T., & Latham, D.W. 2003, ApJ, 591, 397
Green, E. M., Liebert, J., & Saffer, R. A. 2001, in in 12th European Workshop on White Dwarfs, ASP Conf. Ser., Vol. 226, ed. J. L. Provencal, H. L. Shipman, J. MacDonald, and S. Goodchild, (San Francisco: ASP), 192
Han, Z., Podsiadlowski, Ph., Maxted, P.F.L., Marsh, T.R., & Ivanova, N. 2002, MNRAS, 336, 449
Han, Z., Podsiadlowski, Ph., Maxted, P.F.L., & Marsh, T.R. 2003, MNRAS, 341, 669
Han, Z., Podsiadlowski, Ph., & Linas-Gray, 2007, MNRAS, 380, 1098
Heber, U. 2008, in XXI Century Challenges for Stellar Evolution, ed. S. Cassisi & M. Salaris, Mem. Soc. Astr. It., Vol. 79, 375
Hirano, N., Shinnaga, H., Dinh-V., T., Fong, D., Keto, E., Patel, N., Qi, C., Young, K., Zhang, Q, & Zhao, J. 2004, ApJ, 616, L43)
Hjellming, M.S., & Taam, R.E., 1991, ApJ, 370, 709
Huggins, P. J., Mauron, N., & Wirth, E. A. 2009, MNRAS, 396, 1805
Hurley, J.R., Tout, C.A., & Pols, O.R. 2000, MNRAS, 315, 543
Hurley, J.R., Tout, C.A., & Pols, O.R. 2002, MNRAS, 329, 897
Iben, I., Jr., & Livio, M. 1993, PASP, 105, 1373
Iben, I., Jr, & Tutukov, A.V. 1985, ApJS, 58, 661
Ivanova, N., & Podsiadlowski, Ph., 2002, Ap&SS, 281, 191
Ivanova, N., Podsiadlowski, Ph., & Spruit, H. 2002, MNRAS, 334, 819
Izzard, R.G., Jeffery, C.S., & Lattanzio, J. 2007, A&A, 470, 661
Kahn, F. D. & West, K. A. 1985, MNRAS, 212, 837
Kumar, Y. B., & Reddy, B. E. 2009, ApJ, 703, L46
Kwok, S. 1982, ApJ, 258, 280
Kwok, S., Hvrinak, B., & Su, K. Y. L. 2000, ApJ, 544, L149
Lisker et al. 2005, A&A, 430, 223
Lombardi et al. 2002, ApJ, 568, 939
López-Morales M. 2007, ApJ, 660, 732
MacLaurin, C. 1742, A treatise of fluxions, Edinburgh: Ruddimans; Cf. Lang, K. R. 1999, Astrophysical formulae, New York: Springer
Mauron, N. & Huggins, P. J. 2006, A&A, 452, 257
Maxted, P.F.L., Heber, U., Marsh, T.R., & North, R.C. 2001, MNRAS, 326, 1391
Mazeh, T., Goldberg, D., Duquennoy, A., & Mayor, M. 1992, ApJ, 401, 265
Middleditch, J. 2004, ApJ, 601, L167
Miller, G.E., & Scalo, J.M. 1979, ApJS, 41, 513
Moni Biden et al. 2008, in Hot Subdwarf Stars and Related Objects, ASP Conf. Ser., Vol. 392, ed. U. Heber, S. Jeffery, & R. Napiwotski (San Francisco: ASP), 27
Moni Biden, C., Catelan, M., & Altmann, M. 2008, A&A, 480, L1
Morales J. C., Ribas I., Jordi C. 2008, A&A, 478, 507
Morales-Rueda et al. 2006, Balt. Astr., 15, 187
Napiwotzki et al. 2004, Ap&SS, 291, 321
Olofsson, H. 2004, in IAU Symp. 191, Asymptotic Giant Branch Stars, ed. T. le Bertre, A. Lebre, & C. Waelkens (San Franciso: ASP), 325
Palacios et al. 2006, A&A, 453, 261
Podsiadlowski, Ph., Joss, P. C., & Rappaport, S. 1990, A&A, 227, L9
Podsiadlowski, Ph. 2001, in Evolution of Binary and Multiple Star Systems, ASP Conf. Ser., Vol. 229, ed. Ph. Podsiadlowski, S. Rappaport, A. R. King, F. D'Antona, & L. Burderi, (San Francisco: ASP), 239
Politano, M. 1996, ApJ, 465, 338
Politano, M., & Weiler, K.P. 2007, ApJ, 665, 663
Politano, M., Taam, R. E. , van der Sluys, M., & Willems, B.. 2008, ApJ, 687, L99
Pols, O. R., Tout, C. A., Eggleton, P. P., & Han, Z. 1995, MNRAS, 274, 964
Randall et al. 2007, A&A, 476, 1317
Reddy, B. E., & Lambert, D. L. 2005, AJ, 129, 2831
Reed, M.D., & Stiening, R. 2004, PASP, 116, 506
Reimers, D. 1975, Mem. Soc. Roy. Sci. Liege, 6th, ser., 6, 369
Ricker, P. M., & Taam, R. E. 2008, ApJ, 672, L41
Sahai, R., & Bieging, J. H. 1993, AJ, 105, 595
Sahai, R., & Trauger, J. T. 1998, AJ, 116, 1357
Sandquist, E. L., Taam, R. E., & Burkert, A. 2000, ApJ, 533, 984
Sandquist et al. 2000, ApJ, 500, 909
Siess, L., & Livio, M. 1999a, MNRAS, 304, 925
Siess, L., & Livio, M. 1999b, MNRAS, 308, 1133
Sills et al. 1997, ApJ, 487, 290
Sills et al. 2001, ApJ, 548, 323
Soker, N., & Harpaz, A. 2000, MNRAS, 317, 861
Soker, N., & Tylenda, R. 2006, MNRAS, 373, 733
Soker, N., & Harpaz, A. 2007, ApJ, 660, 699
Sweigart, A. V. 1997, ApJ, 474, L23
Taam, R.E., & Sandquist, E.L., 2000, ARA&A, 38, 113
Torres G., Lacy C. H., Marschall L. A., Sheets H. A., & Mader J. A. 2006, ApJ, 640, 1018
Torres, G., Andersen, J., & Gimenez, A. 2009, arXiv:0908.2624v1
Tutukov, A.V., & Yungelson, L.R. 1979, in Mass Loss and Evolution of O-Type Stars, ed. P.S. Conti & W.H. de Loore (Dordrecht: Reidel), 216
Tutukov, A.V., & Yungelson, L.R. 1990, Sov. Astr., 34, 57
Tutukov, A.V., & Yungelson, L.R. 2005, Astr. Rep., 49, 871
van der Sluys, M. V. and Verbunt, F. and Pols, O. R. 2006, A&A, 460, 209
Webbink, R. F. 1976, ApJ, 209, 829
Willems, B., Kolb, U., Sandquist, E.L., Taam, R.E., & Dubus, G. 2005, ApJ, 635, 1263
Yakut, K. & Eggleton, P. P. 2005, ApJ, 629, 1055
Zhao, M. et al. 2009, ApJ, 701, 209